

Article

Computational Modeling of High-Speed Flow of Two-Phase Hydrogen through a Tube with Abrupt Expansion

Konstantin I. Matveev 

Hydrogen Properties for Energy Research (HYPER) Center, School of Mechanical and Materials Engineering, Washington State University, Pullman, WA 99164, USA; matveev@wsu.edu

Abstract: Hydrogen can become a prevalent renewable fuel in the future green economy, but technical and economic hurdles associated with handling hydrogen must be overcome. To store and transport hydrogen in an energy-dense liquid form, very cold temperatures, around 20 K, are required. Evaporation affects the achievable mass flow rate during the high-speed transfer of hydrogen at large pressure differentials, and accurate prediction of this process is important for the practical design of hydrogen transfer systems. Computational fluid dynamics modeling of two-phase hydrogen flow is carried out in the present study using the volume-of-fluid method and the Lee relaxation model for the phase change. Suitable values of the relaxation time parameter are determined by comparing numerical results with test data for high-speed two-phase hydrogen flows in a configuration involving a tube with sudden expansion, which is common in practical systems. Simulations using a variable outlet pressure are conducted to demonstrate the dependence of flow rates on the driving pressure differential, including the attainment of the critical flow regime. Also shown are computational results for flows with various inlet conditions and a fixed outlet state. Field distributions of the pressure, velocity, and vapor fractions are presented for several flow regimes.

Keywords: two-phase hydrogen flow; critical flow regime; cryogenics; computational fluid dynamics; phase-change relaxation model



Citation: Matveev, K.I.

Computational Modeling of High-Speed Flow of Two-Phase Hydrogen through a Tube with Abrupt Expansion. *Hydrogen* 2024, 5, 14–28. <https://doi.org/10.3390/hydrogen5010002>

Academic Editor: Aleksey A. Vedyagin

Received: 12 December 2023

Revised: 17 January 2024

Accepted: 17 January 2024

Published: 18 January 2024



Copyright: © 2024 by the author. Licensee MDPI, Basel, Switzerland. This article is an open access article distributed under the terms and conditions of the Creative Commons Attribution (CC BY) license (<https://creativecommons.org/licenses/by/4.0/>).

1. Introduction

Hydrogen can be produced using renewable energy sources and utilized without emitting harmful pollutants, which makes it one of the most promising clean fuel candidates for the future. However, being the lightest element, hydrogen occupies very large volumes when stored in a gaseous (even highly compressed) form. Liquid hydrogen has the highest gravimetric energy density among all fuels and reasonable volumetric energy density. However, keeping and transferring hydrogen in the liquid form is problematic, as it boils at low cryogenic temperatures, around 20 K near the normal boiling point [1,2]. To develop high-performance practical systems for hydrogen transfer, as well as to properly size safety devices for hydrogen storage, numerical procedures are needed for assessing flow rates of two-phase hydrogen in various system configurations and operational conditions, including the critical flow regimes, when the mass flow rate reaches a maximum and becomes insensitive to further decreases in the outlet pressure for fixed inlet stagnation conditions.

Computational fluid dynamics (CFD) programs can be potentially employed as convenient simulation tools for hydrogen flow prediction [3,4]. However, complete CFD simulations require phase-change models with parameters that need calibration for cryogenic hydrogen. Experimental data for high-speed two-phase hydrogen flow that can be used for such calibrations are rather scarce. Brennan et al. [5] reported experiments for critical flows of two-phase hydrogen in a tube ending with an abrupt expansion into a larger reservoir, and some of their information is used in this work for calibrating one of the phase-change numerical models. Their geometry represents a canonical setup in fluid mechanics, and its variations are commonly encountered in fluid transfer systems.

Smith et al. [6] provided a review of available data for critical flows of two-phase cryogenic fluids. Simoneau and Hendricks [7] conducted critical flow tests of several cryogenics in various nozzle types, but their data are limited to very high pressures (including supercritical states), which are beyond many envisioned applications for liquid hydrogen fueling systems. In these publications, the difficulty of predicting critical flows of cryogenics was noted, as the speed of sound (important for critical flow regimes) may drop significantly in a two-phase mixture in comparison with single-phase substances [8]. Moreover, non-equilibrium thermodynamics effects also play a prominent role in choked flows [9], making the homogeneous equilibrium model (HEM) based on the thermodynamic equilibrium assumption often unsuitable for accurate flow prediction in these situations. Specifically, when a pressurized liquid escapes at a high speed through a short channel to a low-pressure environment, a significant evaporation delay is often present because of limiting transfer rates of heat required for evaporation; hence, nonequilibrium phase-change models are needed to describe this process [10,11].

A number of nonequilibrium reduced-order models have been proposed for critical flow regimes over the years. Henry and Fauske [9] used the basic conservation equations for one-dimensional isentropic flow in converging nozzles to derive an expression for the critical pressure ratio and flow rate. As the thermodynamic equilibrium model underpredicted the critical flow rates, they argued that there is little time for evaporation to take place in a high-speed flow over a short distance, so a correction is needed for the mass flow rate in situations with low qualities at the inlet. The model with the proposed correction demonstrated an approximate agreement with test data from various critical-flow experiments.

Lee [12] developed a semi-implicit numerical scheme for solving two-phase flow problems with delayed phase change. They employed a simple relaxation-type model, where the evaporation and condensation rates were proportional to the normalized difference between the saturated and actual temperature and the density of the locally diminishing phase. The numerical coefficient in the phase-change rate of that model is effectively the inverse value of the relaxation time, which can be assessed by comparing numerical predictions to the experimental results. This model has been utilized in many computational studies since then by various researchers and is selected for the current study. Another popular choice for evaporation and condensation in numerical simulations is the homogeneous relaxation model, commonly abbreviated as HRM [13]. Downar-Zapolski et al. [14] presented more elaborate forms for the relaxation times that included vapor fractions and ratios of pressure differences involving actual pressure, as well as saturated and critical pressures. Different forms were recommended for low- and high-pressure flows, and several constants in these correlations were obtained by fitting numerical results to test data from highly controlled, well-measured “Moby Dick” experiments that involved critical flows of liquid water and vapor [15,16]. While the HRM model was initially developed and applied for quasi-one-dimensional flows, Schmidt et al. [17] extended this model to three dimensions.

More recently, other models with delayed or slower phase change and assuming the presence of metastable states have been proposed for homogeneous two-phase cryogenic flows. For example, Travis et al. [18] used an equation of state based on Helmholtz free energy and introduced a non-equilibrium parameter relating liquid and vapor temperatures to show a reasonable agreement with the high-pressure NASA test data of Simoneau and Hendricks [7]. Venetsanos [19] developed a hybrid model combining the homogeneous equilibrium model (HEM) and homogeneous frozen model (HFM) and also demonstrated a comparison with NASA data. Wilhelmsen and Aasen [20] presented a delayed homogeneous relaxation model and the metastable isentrope model and found that the critical flow rate is mainly affected by the achievable degree of metastability. It can be noted that besides the volumetric phase-change models suitable for homogeneous flows, there are approaches based on the liquid–vapor interface [4,21]. However, these models require identification and tracking of the free surface and thus are very expensive for flows that contain a number of small bubbles or droplets.

To simulate high-speed, two-phase hydrogen flows in practical conduits (that are generally more complex than simple nozzles) using computational fluid dynamics (CFD), it is beneficial to employ relatively simple finite-rate phase-change formulations with a few numerical parameters that can be evaluated from a comparison with test data. The purpose of the present work is to determine suitable relaxation parameters in the Lee model by comparing CFD and experimental results for a fast two-phase hydrogen flow [5]. This numerical calibration is accomplished by varying a relaxation time parameter to match several reported measurements. The computational aspects and the current numerical procedure are discussed in the next two sections. They are followed by a calibration study used to obtain estimates for the relaxation time parameter by comparing computational results with experimental parameters. Additional simulations are also conducted to demonstrate the attainment of critical flow regimes in the same setup by varying the outlet pressure and to show the flow rate's dependence on the inlet conditions for the fixed outlet pressure.

2. Computational Modeling Aspects

The modeling of high-speed two-phase hydrogen flows with evaporation and condensation is accomplished in this study using the computational fluid dynamics (CFD) software Simcenter Star-CCM+ version 2022.1, which employs a finite-volume viscous solver. The first-order stepping in time and the second-order discretization in space are selected. The governing integral-form fluid dynamics equations for the mass, momentum, and energy implemented in this solver can be written as follows [22]:

$$\frac{\partial}{\partial t} \int_V \rho dV + \oint_A \rho \mathbf{v} \cdot d\mathbf{a} = \int_V \sum_i S_{\beta i} \rho_i dV, \quad (1)$$

$$\frac{\partial}{\partial t} \int_V \rho \mathbf{v} dV + \oint_A \rho \mathbf{v} \otimes \mathbf{v} \cdot d\mathbf{a} = - \oint_A p \mathbf{I} \cdot d\mathbf{a} + \oint_A \mathbf{T} \cdot d\mathbf{a} + \int_V \mathbf{f}_b dV, \quad (2)$$

$$\frac{\partial}{\partial t} \int_V \rho E dV + \oint_A (\rho E + p) \mathbf{v} \cdot d\mathbf{a} = - \oint_A \dot{\mathbf{q}} \cdot d\mathbf{a} + \oint_A (\mathbf{T} \cdot \mathbf{v}) \cdot d\mathbf{a} + \int_V \mathbf{f}_b \cdot \mathbf{v} dV + \int_V S_E dV, \quad (3)$$

where ρ , p , and \mathbf{v} are the fluid density, pressure, and velocity, respectively; V , A , and \mathbf{a} are the numerical cell volume, surface area, and surface-area vector, respectively; $S_{\beta i}$ is the source term of phase i ; \mathbf{I} is the unity tensor; \mathbf{T} is the viscous stress tensor; \mathbf{f}_b is the body force; E is the total energy per unit mass; $\dot{\mathbf{q}}$ is the heat flux vector; and S_E is the energy source term.

For modeling the turbulent effects, the realizable $k - \varepsilon$ model [23] was applied in most simulations (the SST $k - \omega$ model and the Reynolds stress model were also tried, but they produced very similar results, within 1% of the realizable $k - \varepsilon$ model). The governing transport equations for the turbulent kinetic energy k and the turbulent dissipation rate ε in this model can be written as follows:

$$\frac{\partial(\rho k)}{\partial t} + \frac{\partial(\rho k u_j)}{\partial x_j} = \frac{\partial}{\partial x_j} \left[\left(\mu + \frac{\mu_t}{\sigma_k} \right) \frac{\partial k}{\partial x_j} \right] + G_k - \rho \varepsilon, \quad (4)$$

$$\frac{\partial(\rho \varepsilon)}{\partial t} + \frac{\partial(\rho \varepsilon u_j)}{\partial x_j} = \frac{\partial}{\partial x_j} \left[\left(\mu + \frac{\mu_t}{\sigma_\varepsilon} \right) \frac{\partial \varepsilon}{\partial x_j} \right] + \rho C_{\varepsilon 1} S \varepsilon - \rho C_{\varepsilon 2} \frac{\varepsilon^2}{k + \sqrt{\nu \varepsilon}}, \quad (5)$$

where G_k is the turbulent kinetic energy generation term due to the mean velocity gradients, $S = \sqrt{2 S_{ij} S_{ij}}$ is the scalar invariant of the strain rate tensor $S_{ij} = \frac{1}{2} \left(\frac{\partial u_i}{\partial x_j} + \frac{\partial u_j}{\partial x_i} \right)$, ν is the kinematic viscosity, $C_{\varepsilon 1}$ and $C_{\varepsilon 2}$ are the model coefficients, and σ_k and σ_ε are the turbulent Prandtl numbers. The turbulent viscosity μ_t is given as

$$\mu_t = \rho C_\mu \frac{k^2}{\varepsilon}, \quad (6)$$

where C_μ depends on turbulent properties and mean flow [24].

To model a two-phase liquid–gas flow, the volume-of-fluid (VOF) method has been employed [25], involving the High-Resolution Interface Capturing (HRIC) scheme. The effective fluid density ρ and viscosity μ are calculated from the vapor and liquid properties:

$$\rho = \rho_{vap}\beta_{vap} + \rho_{liq}(1 - \beta_{vap}), \quad (7)$$

$$\mu = \mu_{vap}\beta_{vap} + \mu_{liq}(1 - \beta_{vap}), \quad (8)$$

where β_{vap} is the vapor volume fraction, whose evolution is described by the following equation:

$$\frac{\partial}{\partial t} \int_V \beta_i dV + \int_A \beta_i \mathbf{v} \cdot d\mathbf{a} = \int_V \left(S_{\beta_i} - \frac{\beta_i}{\rho_i} \frac{D\rho_i}{Dt} \right) dV, \quad (9)$$

where $D\rho_i/Dt$ is the material derivative of phase densities. The present approach for multiphase flow modeling has been extensively validated [26,27].

The evaporation and condensation rates are implemented in the present work using the Lee model [12]:

$$\dot{\rho}_{evap} = \frac{\rho_{liq}}{\tau} \frac{T - T_{sat}}{T_{sat}}, \quad \text{if } T > T_{sat}, \quad (10)$$

$$\dot{\rho}_{cond} = \frac{\rho_{vap}}{\tau} \frac{T_{sat} - T}{T_{sat}}, \quad \text{if } T < T_{sat}, \quad (11)$$

where T is the local temperature, T_{sat} is the local saturation temperature, and τ is the relaxation time parameter determined from the comparison of CFD results with experimental data. The phase change is implemented in the software through vapor and liquid mass sources by entering expressions from Equations (10) and (11), as the Lee model is not a built-in option in the employed software. These source options are available in the software when a multi-species setting is chosen for each phase (although only one species can still be used). They affect the mass, energy, and volume fraction transport equations. More detailed information on the theoretical formulations and additional references can be found in the software manual [28].

The hydrogen properties for both vapor and liquid phases are obtained from CoolProp software version 6.6.0 [29,30] and imported as tables into the CFD program. The numerical time step used in the current study is 10^{-5} s. No significant dependence on the time step in steady-state regimes has been identified for Δt in the range of 10^{-4} – 10^{-5} s for several case studies. At larger time steps, numerical simulations often diverge. Although the present simulations are unsteady, only steady-state results are reported when the mean flow properties no longer evolve. The reason for using more elaborate transient simulations is that it is very difficult to obtain a steady-state solution with a steady solver since simulations can easily diverge for complex (compressible, phase-changing, fast) flows even with a small time step unless the initial guesses for all flow-field properties are close to actual steady-state solutions.

3. Computational Setup

The geometrical setup in this study corresponds to the system employed by Brennan et al. [5] for experimentally determining critical flow rates of two-phase cryogenics. The entire system includes a pressurized liquid hydrogen tank from which hydrogen flows through a transfer line with several components and then a tube to an expansion chamber maintained at low pressure (Figure 1a). They reported mass fluxes, stagnation enthalpy, and pressure values measured at the tube exit plane and inside the expansion chamber. As the information for the complete system geometry is not available, only a part of the entire system is modeled here, including a section of the tube (whose diameter was given as 8.44 mm) and a portion of the expansion chamber (Figure 1). The modeled system dimensions are shown in Figure 1b. For computational economy, only a quarter of the considered tube and chamber volumes were utilized to form the numerical domain

with two symmetry planes passing through the centerlines of the tube and the chamber (Figure 2). Although the most important experimental portion (the tube and its immediate vicinity in the expansion chamber) has nearly axisymmetric geometry, the flow may have had a more complex structure (no test data are available), and the truncated numerical domain may not capture all three-dimensional flow features.

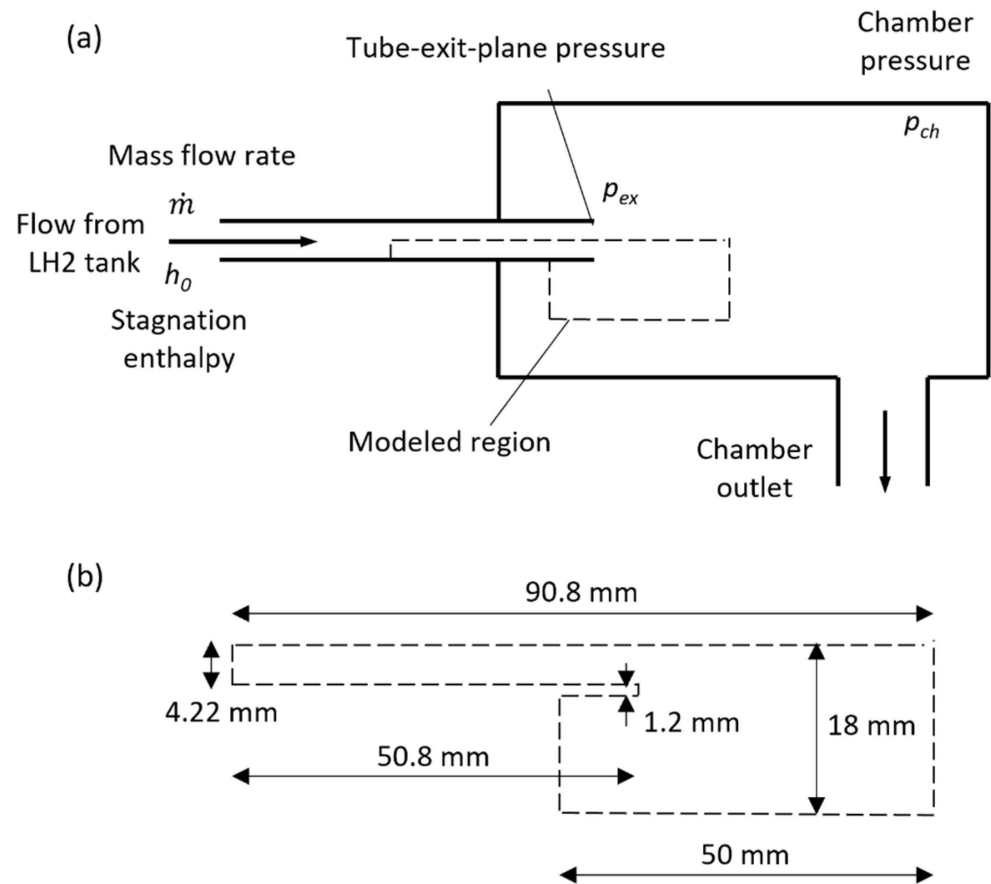


Figure 1. (a) Schematic of the system with variables reported in experiments. (b) Side plane of the numerical domain with dimensions.

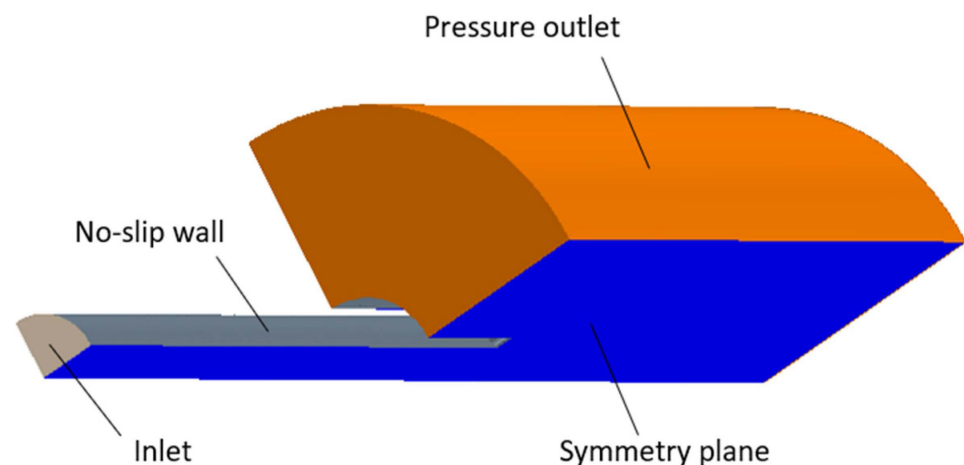


Figure 2. Numerical domain with boundary conditions.

The boundary conditions in the numerical setup include the pressure (or flow rate in some simulations), temperature, and volume fraction of liquid hydrogen at the inlet and outlet, as well as no-slip walls on the tube surface (Figure 2). However, most of these parameters were not directly measured in the experiments. As the mass flow rate was

known in the tests, the mass flow inlet was employed at the tube entrance for simulating experimental conditions, while the liquid volume fraction was selected to maintain the total enthalpy at a prescribed (experimental) value. An experimentally measured pressure in the expansion chamber was used as the boundary condition at the outlet, and the outlet temperature was taken at the corresponding saturation value. Steady-state flow regimes were obtained for a set of relaxation time values. The numerically evaluated tube's exit-plane pressure values were then compared with the experimental data point to determine which relaxation time provides the best fit.

Another set of simulations was carried out to demonstrate a dependence of the mass flow rate on the driving pressure difference, including the achievement of a critical flow rate when the mass flow rate stops changing with increasing pressure difference. In these cases, the outlet pressure was varied, whereas a stagnation inlet with the fixed conditions of one of the test cases was used. Additional simulations were also conducted with a variable inlet pressure. In these scenarios, the outlet pressure was kept constant, whereas the inlet boundary conditions were varied. More detailed information about boundary conditions is given in the next section.

A trimmed numerical mesh, consisting primarily of hexahedral cells, was generated in the numerical domain (Figure 3). Several prism layers were placed near the tube wall, and a refinement was added near the tube exit, whereas a coarser mesh was constructed in the expansion chamber that only weakly affects flow through the tube. The cell dimensions near the tube wall were selected to make the Y^+ values for the tube flow between 30 and 100, thus relying on the wall function approach for modeling the boundary layer.

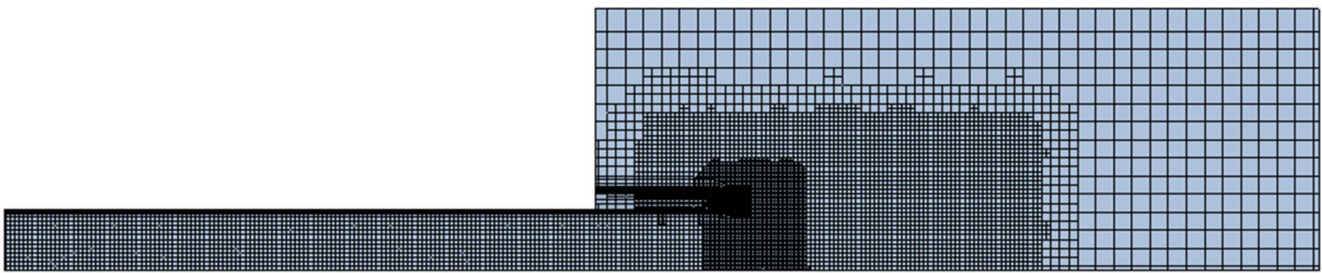


Figure 3. Fine numerical mesh at the symmetry plane of the numerical domain. Total cell count is 117,914, and the cell size at the tube exit is 0.16 mm.

4. Results

Several simulation series have been carried out in this study. Table 1 lists these simulations with corresponding boundary conditions that are discussed in the following subsections. Series #1 covers the calibration cases, including the mesh-verification study. In series #2, the outlet pressure is varied. This series includes a demonstration of the critical flow attainment. Series #3 presents a study with a variable inlet pressure and a fixed inlet liquid volume fraction. In series #4, the inlet pressure is also varied, but the fixed inlet parameter is a total enthalpy.

Table 1. Simulation sequences and corresponding boundary conditions.

Simulation Series	Inlet Boundary Conditions	Outlet Boundary
Series #1 Calibration study for three test conditions	Mass flow inlet: (i) Mass flow rate is assigned an experimental value (ii) Temperature is saturated for two-phase flow (b,c) or selected to keep the given total enthalpy for the inlet subcooled liquid state (a): (a) $T_{in} = 24.5$ K, (b) $T_{in} = 24.3$ K, (c) $T_{in} = 27.0$ K (iii) Liquid volume fraction is selected either to produce h_0 for two-phase flow or to be one for subcooled liquid: (a) $\beta_{liq} = 1$, (b) $\beta_{liq} = 0.571$, (c) $\beta_{liq} = 0.623$	Pressure outlet: (a) $P_{out} = 168$ kPa (b) $P_{out} = 116$ kPa (c) $P_{out} = 135$ kPa
(a) $\dot{m} = 5.33 \times 10^3$ kg/(s·m ²), $h_0 = 5.27 \times 10^4$ kJ/kg;		
(b) $\dot{m} = 2.40 \times 10^3$ kg/(s·m ²), $h_0 = 6.34 \times 10^4$ kJ/kg;		
(c) $\dot{m} = 3.23 \times 10^3$ kg/(s·m ²), $h_0 = 1.09 \times 10^5$ kJ/kg		

Table 1. Cont.

Simulation Series	Inlet Boundary Conditions	Outlet Boundary
Series #2 Variable outlet pressure study	Stagnation inlet: $P_0 = 522$ kPa, $T_0 = 24.7$ K, $\beta_{liq} = 1$	Pressure outlet: P_{out} is varied between 152 kPa and 522 kPa
Series #3 Variable inlet pressure study with constant inlet liquid volume fraction 0.571	Pressure inlet: (i) P_{in} is varied between 131 kPa and 338 kPa (ii) Temperature is saturated (iii) $\beta_{liq} = 0.571$	Pressure outlet: $P_{out} = 116$ kPa
Series #4 Variable inlet pressure study with constant inlet total enthalpy 6.3×10^4 J/kg	Pressure inlet: (i) P_{in} is varied between 163 kPa and 361 kPa (ii) Temperature is saturated (iii) Liquid volume fraction is selected to maintain given total enthalpy	Pressure outlet: $P_{out} = 116$ kPa

4.1. Verification and Calibration Study (Series #1)

A mesh-verification study was conducted for one test condition, corresponding to the experimentally reported stagnation enthalpy of 5.27×10^4 kJ/kg, the tube exit plane pressure of 220 kPa, the outlet pressure of 168 kPa, and the mass flux of 5.33×10^3 kg/(s \times m²). As the mass flow rate was known, the mass flow inlet was employed at the tube entrance for simulating these experimental conditions. Since the liquid at the entrance was subcooled in this case, the temperature was selected to produce the given total enthalpy, while using an inlet liquid volume fraction of 1. With the evolution of the flow (e.g., starting from a small flow rate and gradually increasing it to the given test value), the inlet pressure and the corresponding inlet temperature also evolved until they settled in a stable state. In such a state, the stagnation enthalpy reached the experimental value from [5].

For the mesh-verification study, the relaxation time in the phase-change model was chosen as $\tau = 7.5 \times 10^{-5}$ s, which produced a reasonably good match to the test data point for the tube exit pressure, as shown below. Three numerical grids of different mesh densities were generated, and the tube exit pressure was evaluated from the steady-state solutions. Numerical results for this pressure obtained on different grids are summarized in Table 2, demonstrating the monotonic convergence of results with increasing mesh refinement.

Table 2. Grid characteristics and computed tube exit plane pressure.

Mesh	Cell Count	Cell Size near Tube Exit	Tube Exit Pressure
Coarse	8999	0.62 mm	182.8 kPa
Medium	24,540	0.31 mm	213.4 kPa
Fine	117,914	0.16 mm	220.1 kPa

The numerical uncertainty is assessed using the standard procedure [31]. First, the Richardson correction to the fine-mesh solution is determined as follows [22]:

$$\delta_{RE} = \frac{\Delta_{12}}{2^{p_{ob}} - 1}, \quad (12)$$

where Δ_{12} is the difference between solutions of the fine and medium meshes, and p_{ob} is the observed order of accuracy defined by the following equation:

$$p_{ob} = \frac{\log(\Delta_{23}/\Delta_{12})}{\log(\beta)}, \quad (13)$$

where Δ_{23} is the difference between solutions of the medium and coarse meshes, and β is the ratio of linear dimensions of numerical cells between the grids, which is equal to 2 in the present study. To assess the numerical uncertainty U , the Richardson correction δ_{RE} is additionally multiplied by the factor of safety F [31]:

$$U = F\delta_{RE}. \quad (14)$$

The calculated numerical uncertainty comes to about 1.1% of the pressure value computed on the fine mesh. Given the small difference between the prediction on the fine mesh and measured pressure values (less than 1%), the current numerical modeling approach is deemed acceptable.

Using the fine mesh from the verification study, calibration studies were conducted with several relaxation times for three experimental cases to determine what values of τ lead to better agreement between the numerically determined and experimentally measured tube exit plane pressure values, while imposing the experimental boundary conditions in the numerical simulations (which do not involve the tube exit plane pressure). In regimes with two-phase flow at the inlet, the inlet temperature was chosen as saturated at the inlet pressure. A look-up table for the inlet liquid volume fraction was prepared in advance as a function of inlet pressure and the given (experimental) values for the total enthalpy and mass flow rate, and this volume fraction was used as one of the boundary conditions.

The resulting dependence of the tube exit pressure p_{ex} on τ is shown in Figure 4 for three test cases from [5]. In all of them, the tube exit pressure decreases with increasing the relaxation time. For the studied conditions, the best-fit τ values change between about 5×10^{-5} s and 20×10^{-5} s, with higher numbers corresponding to larger vapor content (and enthalpy) in the inlet flow. Hence, the relaxation times in these brackets can be suggested as reasonable estimates for simulating hydrogen flows in the considered range of conditions.

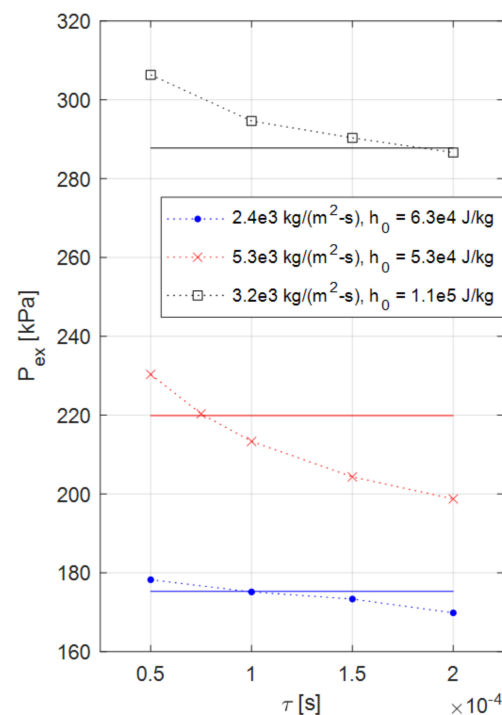


Figure 4. Tube exit pressure for three experimental cases. Symbols and dotted lines, numerical results; solid horizontal lines, test values.

To illustrate flow properties in cases with different mass fluxes and stagnation enthalpies, the field distributions of the pressure, vapor volume fraction, and velocity are given in Figures 5–7 and variations of these properties along the tube centerline are shown in Figure 8. The relaxation times of 7.5×10^{-5} , 10×10^{-5} , and 20×10^{-5} s are chosen for the situations with mass fluxes 2.4×10^3 , 5.3×10^3 , and 3.2×10^3 kg/(s \times m²), respectively, as they produced the closest agreement with test results for the tube exit pressure. From the flow-field images and axial-line plots in Figure 8, one can observe the presence of high pres-

sure at the tube inlet, which gradually decreases toward the tube exit. An abrupt pressure drop occurs right after the tube exit plane with partial pressure recovery taking place at about one tube diameter downstream. The strongest pressure increase, resembling a shock wave, and several expansion and compression cells are noticeable for the highest-enthalpy case (Figures 7 and 8), while the downstream cells become less pronounced at lower flow enthalpies. Outside of the jet, the pressure varies little in the expansion chamber.

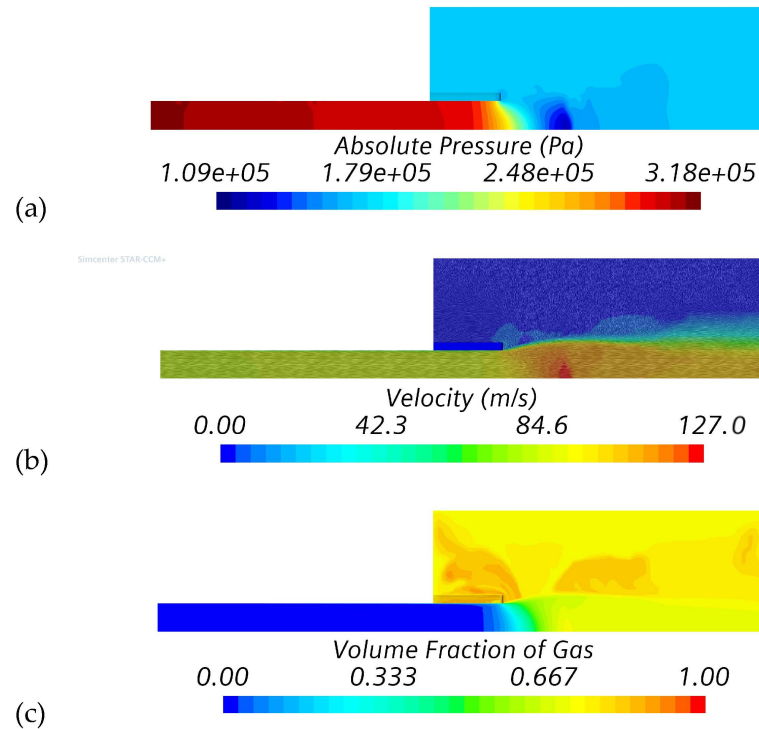


Figure 5. Field distributions of (a) pressure, (b) velocity, and (c) vapor volume fraction at the condition with mass flux of $5.33 \times 10^3 \text{ kg}/(\text{s} \times \text{m}^2)$ and stagnation enthalpy of $5.27 \times 10^4 \text{ J}/\text{kg}$.

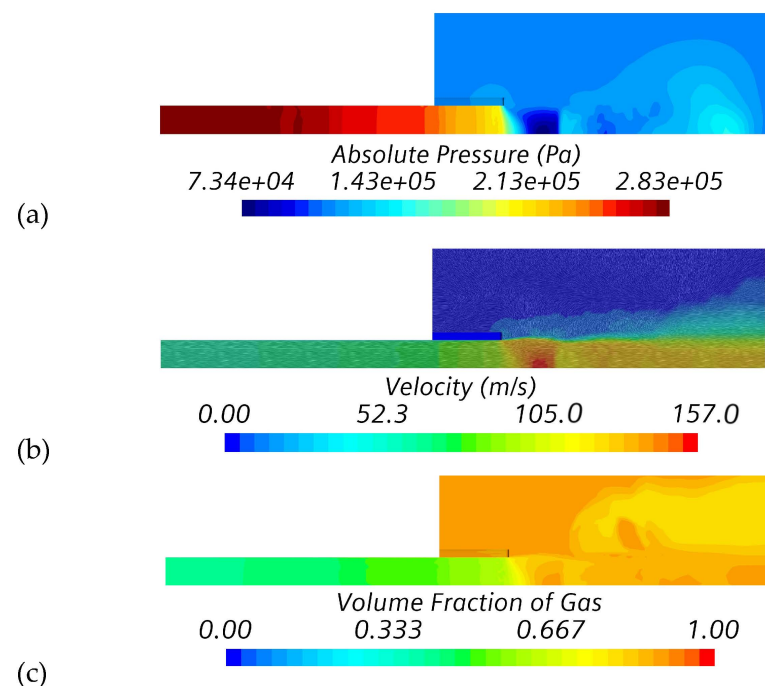


Figure 6. Field distributions of (a) pressure, (b) velocity, and (c) vapor volume fraction at the condition with mass flux of $2.40 \times 10^3 \text{ kg}/(\text{s} \times \text{m}^2)$ and stagnation enthalpy of $6.34 \times 10^4 \text{ J}/\text{kg}$.

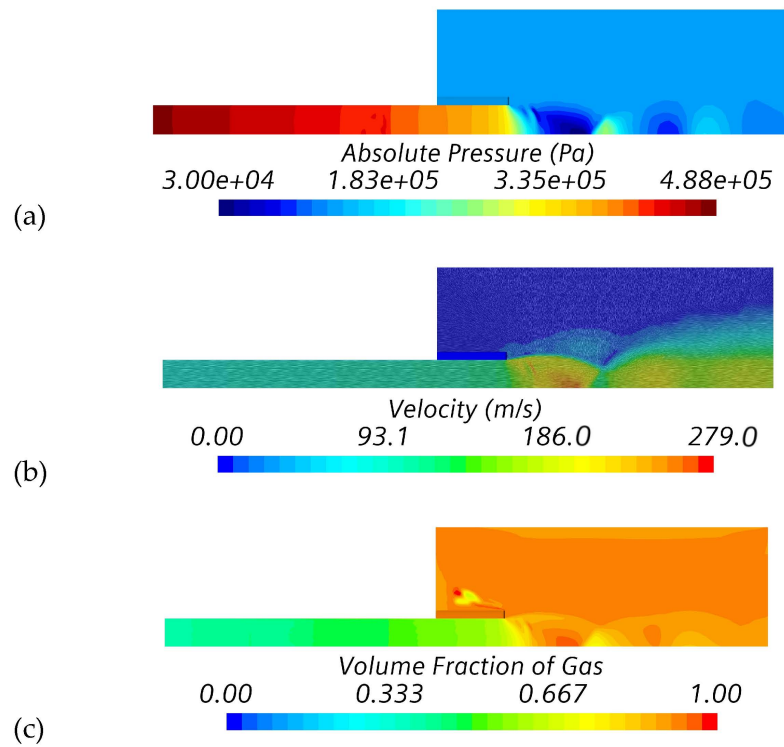


Figure 7. Field distributions of (a) pressure, (b) velocity, and (c) vapor volume fraction at the condition with mass flux of $3.23 \times 10^3 \text{ kg}/(\text{s} \times \text{m}^2)$ and stagnation enthalpy of $1.09 \times 10^5 \text{ J}/\text{kg}$.

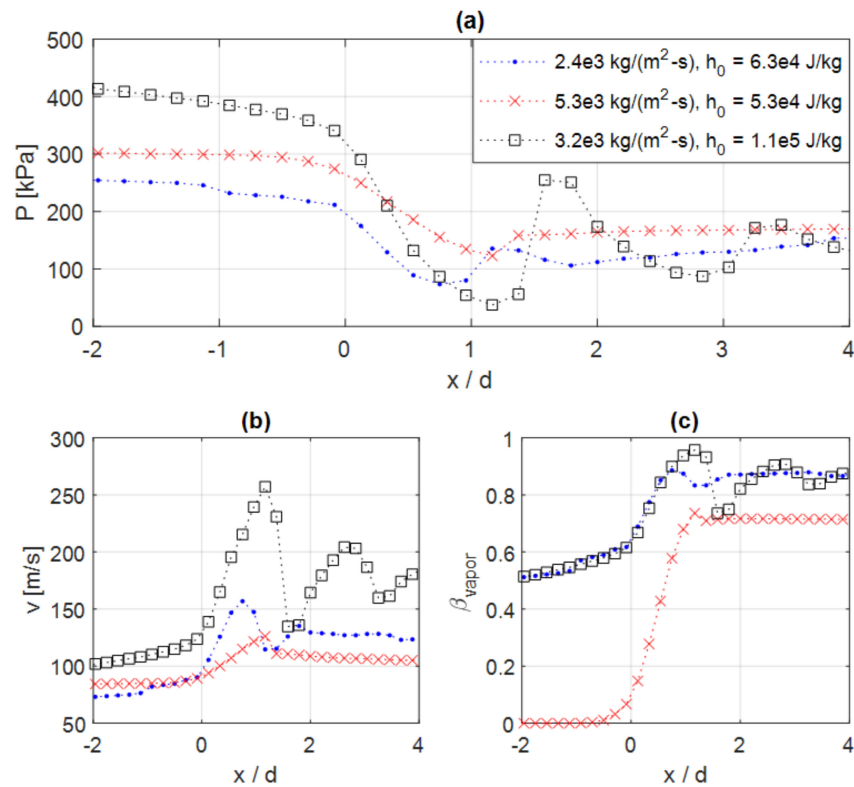


Figure 8. Distributions of (a) pressure, (b) velocity magnitude, and (c) vapor volume fraction along the tube centerline for three calibration cases. The horizontal coordinate is normalized by the tube diameter d . $x = 0$ corresponds to the tube exit plane.

The velocity is more or less uniform in the tube beyond thin boundary layers at the tube walls (Figures 5b, 6b and 7b). The velocity magnitudes reach maxima after the tube exit (Figure 8b), correlating with the pressure drop (Figure 8a), whereas intensive evaporation expands the fluid (Figure 8c). A growing jet is formed further downstream, which entrains surrounding fluid (Figures 5b, 6b and 7b). The vapor fraction in the tube depends on a specific case. For example, the inlet fluid at the lowest enthalpy (and the highest mass flux) is completely in the liquid form (Figures 5 and 7c), and it starts evaporating only near the tube exit. In the other cases, the fluid has a large vapor fraction at the inlet (Figures 6, 7c and 8c), and the phase change continues throughout the tube. Intensive evaporation occurs at the tube exit, followed by partial re-condensation and smaller phase variations in the expansion chamber.

4.2. Variable Outlet Pressure Study (Series #2)

To illustrate the variation in the flow rate as a function of the pressure differential between the inlet and outlet, including the attainment of the critical flow regime, parametric simulations were conducted using the stagnation inlet type in CFD software. Specifically, the same stagnation pressure and temperature (5.22×10^5 Pa and 24.72 K) were selected as in the mesh-verification case, and the inlet liquid volume fraction was chosen as 1 (sub-cooled state). The pressure boundary was used at the outlet of the numerical domain, and this pressure value was treated as a variable parameter. A relaxation time of 7.5×10^{-5} s was employed in this parametric study as it provided a good agreement with test data for the zero-vapor-fraction inlet state (Figure 4). The results for variable outlet pressure were obtained in a sequence of simulations. In the initial state, the pressure was uniform in the entire domain, including all boundaries, and was equal to the inlet stagnation pressure. Then, the outlet pressure was gradually reduced to some value, at which the solution was allowed to settle and the numerical values for the variables of interest (e.g., mass flux) were recorded. Then, the outlet pressure was changed again to reach the next state, and so on. A similar procedure is used in the other parametric studies in this paper.

The results for the mass flux \dot{m}/A (with \dot{m} and A being the mass flow rate and the tube cross-sectional area, respectively) as a function of the difference between the stagnation inlet pressure and the outlet static pressure, $\Delta P = P_{stag} - P_{out}$, are shown in Figure 9. With an increase in ΔP at low-pressure differentials, the flow rate increases with pressure differential, whereas the rate of growth gradually decreases. For ΔP in the range of 200–300 kPa, the mass flux exhibits fluctuations with amplitude around ± 200 kg/(s \times m²). After ΔP exceeds 300 kPa, the flow rate stops responding to further drops in the downstream pressure. This corresponds to the critical flow regime when the downstream conditions no longer affect the inlet flow.

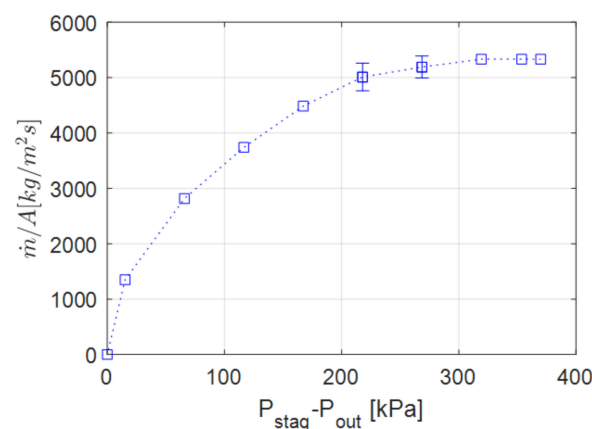


Figure 9. Mass flux of hydrogen flowing through the tube at variable outlet pressure. Error bars at $200 \text{ kPa} < \Delta P < 300 \text{ kPa}$ indicate fluctuations observed in these regimes.

Illustrations of flow properties for low and high (but still subcritical) pressure differentials are given in Figures 10 and 11. At a small ΔP with mass flux $1.35 \times 10^3 \text{ kg}/(\text{s} \times \text{m}^2)$, there is a gradual pressure variation in the tube and near-constant pressure in the chamber (Figure 10). The velocity in the jet exiting the tube is more regular in comparison with the previous cases (Figures 5–7). The evaporation is practically absent in this specific case with a slow flow and small pressure variation, so the liquid occupies the entire domain.

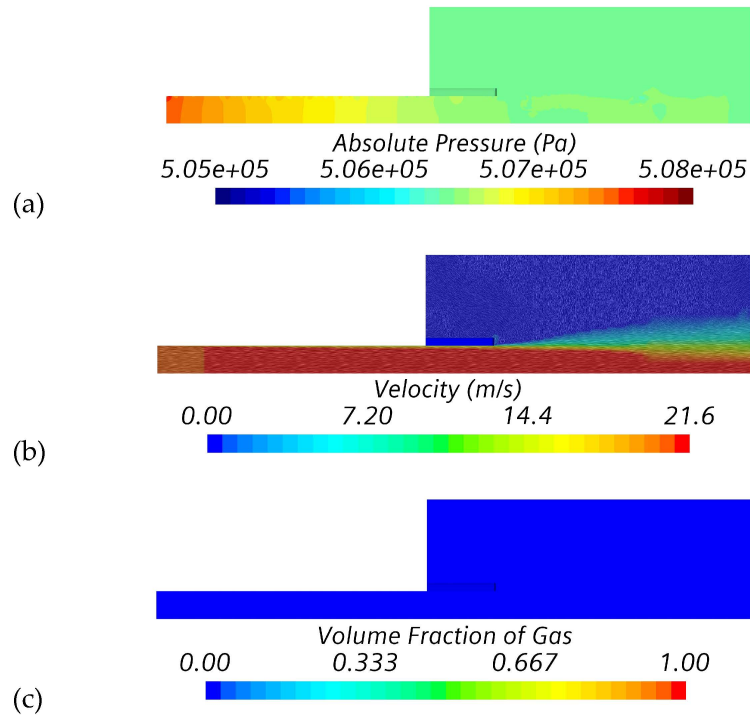


Figure 10. Field distributions of (a) pressure, (b) velocity, and (c) vapor volume fraction at the condition with mass flux of $1.35 \times 10^3 \text{ kg}/(\text{s} \times \text{m}^2)$ and stagnation enthalpy of $5.3 \times 10^4 \text{ J}/\text{kg}$.

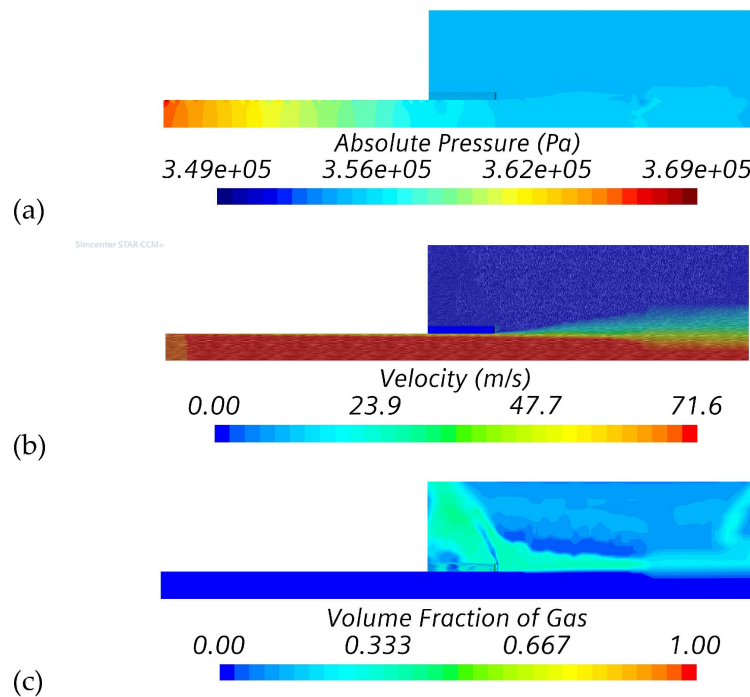


Figure 11. Field distributions of (a) pressure, (b) velocity, and (c) vapor volume fraction at the condition with mass flux of $4.48 \times 10^3 \text{ kg}/(\text{s} \times \text{m}^2)$ and stagnation enthalpy of $5.3 \times 10^4 \text{ J}/\text{kg}$.

At a larger subcritical mass flux of $4.48 \times 10^3 \text{ kg}/(\text{s} \times \text{m}^2)$, there is more significant pressure variation, including inside the expansion chamber (Figure 11), while the velocity field is similar to that at lower ΔP but of higher magnitudes. Evaporation takes place in the chamber but remains insignificant inside the tube and in the jet portion close to the tube exit.

4.3. Variable Inlet Pressure Studies (Series #3 and #4)

Another parametric variation of interest involves a change in the inlet state when the outlet conditions are fixed. Simulations of this kind have been conducted for two scenarios, corresponding to computational series #3 and #4 in Table 1. In series #3, the inlet vapor fraction was maintained at the same level of 0.571 (as in one of the test cases with the flow rate of $2.4 \times 10^3 \text{ kg}/\text{s} \times \text{m}^2$), whereas the pressure inlet was employed using the inlet static pressure as a variable parameter. The inlet temperature was equal to the saturated temperature at the given pressure. The pressure boundary was used at the domain outlet, and the outlet pressure was fixed at $1.16 \times 10^5 \text{ Pa}$. The flow rate and the total enthalpy were the output variables (recorded for steady-state flow conditions). In series #4, the inlet pressure was varied as well, whereas the temperature was equal to the saturated temperature, and the inlet liquid volume fraction was adjusted to maintain the constant total flow enthalpy at $6.3 \times 10^4 \text{ J}/\text{kg}$. The outlet pressure was again fixed at the same value as in the first series.

The dependencies of the mass flow rate on the difference between the inlet and outlet pressure for these two scenarios are given in Figures 12a,b, respectively. Also shown in this figure are the variations in the inlet total enthalpy in the first case (Figure 12c) and the inlet liquid volume fraction in the second case (Figure 12d). When the liquid fraction reaches 1 (Figure 12d) in series #4, the inlet temperature is chosen below the saturation value to keep the total enthalpy the same, which implies the presence of subcooled liquid at the inlet in such a regime. Points shown in Figure 12 were obtained in a sequence of simulations, where the inlet pressure was gradually varied from one value to another.

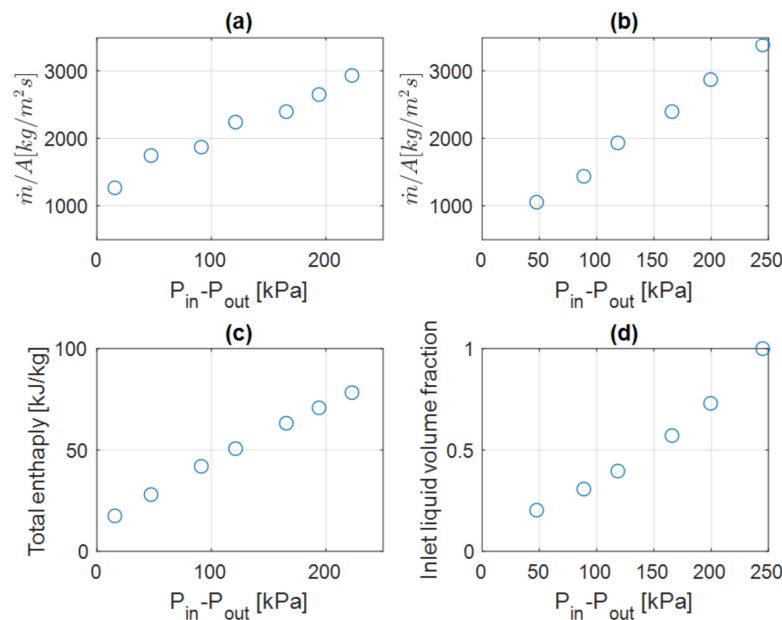


Figure 12. (a,b) Mass flow rates as functions of static pressure differential: (a) constant inlet liquid fraction—series #3; (b) constant total enthalpy—series #4. (c) Variation in total enthalpy with inlet liquid fraction of 0.571 (series #3). (d) Variation in inlet liquid fraction with total enthalpy of $6.3 \times 10^4 \text{ J}/\text{kg}$ (series #4).

In these studies, the mass flow rate is found to increase with increasing pressure differential without achieving saturation in the considered range for both scenarios (Figure 12a,b), as the inlet total enthalpy in the first case and the inlet liquid fraction in the second case

continue increasing, while the critical flow rate depends on the inlet state. The flow rate variation is more linear for the second case (Figure 12b). The total inlet enthalpy is found to be linearly proportional to the inlet pressure for the fixed liquid fraction situation. In the second scenario, the inlet liquid fraction increases with the pressure difference from almost zero (vapor-dominated flow) to one (liquid only). These numerical assessments can be useful for predicting mass flow rates of two-phase hydrogen for variable inlet states when the ambient or downstream conditions remain the same.

5. Conclusions

Computational fluid dynamics simulations have been conducted for critical and subcritical flows of two-phase hydrogen in a tube configuration with abrupt expansion at the exit. This setup is similar to components used in many practical systems. After the mesh-verification studies, a relaxation time parameter in the Lee phase-change models was varied, and the flow rate predictions were compared with test data. The relaxation times between 5×10^{-5} and 20×10^{-5} s were found to produce a reasonable correlation with experimentally measured pressure at the tube exit plane for mass fluxes between 2×10^3 and 5×10^3 kg/(s \times m²) and stagnation enthalpies between 0.5×10^5 and 1.1×10^5 J/kg. The dependence of the flow rate on the driving pressure differential (while keeping the inlet condition the same) was simulated for one of the cases. At lower pressure differences, the flow rate increased with the pressure difference, whereas at a sufficiently high pressure differential, the flow rate became insensitive to further drops in the outlet pressure, indicating the attainment of the critical flow regime. In the transition regime before reaching such a state, the flow rate exhibited moderate fluctuations. In the scenarios with the fixed outlet state and variable inlet conditions (either the total enthalpy or the liquid volume fraction), the mass flow rate increased with the driving pressure differential roughly linearly in the studied ranges. The relaxation time values obtained in this study can be suggested for CFD modeling of similar systems with two-phase hydrogen flow.

In the future, by using greater computational resources and more complete descriptions of experimental systems, one can simulate larger flow domains starting from the stagnated regions down to the system exit, thus reducing uncertainties associated with a truncated modeling domain. More experiments with high-speed two-phase hydrogen flows in other geometrical configurations will be useful for providing more data for complete validation of the numerical models.

Funding: This research was funded by the U.S. National Science Foundation, grant number 2214235.

Data Availability Statement: The data presented in this study are openly available in article.

Acknowledgments: The author thanks Jacob Leachman of Washington State University for valuable discussions on the subject of this paper.

Conflicts of Interest: The author declares no conflicts of interest.

References

1. Matveev, K.I.; Leachman, J.W. The effect of liquid hydrogen tank size on self-pressurization and constant-pressure venting. *Hydrogen* **2023**, *4*, 444–455. [[CrossRef](#)]
2. Stolten, D.; Emonts, B. *Hydrogen Science and Engineering: Materials, Processes, Systems and Technology*; Wiley: Weinheim, Germany, 2016.
3. Matveev, K.I.; Leachman, J.W. Modeling of liquid hydrogen tank cooled with para-orthohydrogen conversion. *Hydrogen* **2023**, *4*, 146–153. [[CrossRef](#)]
4. Kartuzova, O.; Kassemi, M. Self-pressurization and spray cooling simulations of the multipurpose hydrogen test bed (MHTB) ground-based experiment. In Proceedings of the AIAA/ASME/SAE/ASEE Joint Propulsion Conference, Cleveland, OH, USA, 28–30 July 2014.
5. Brennan, J.A.; Edmonds, D.K.; Smith, R.V. *Two-Phase (Liquid-Vapor), Mass-Limiting Flow with Hydrogen and Nitrogen*; Technical Note 359; National Bureau of Standards: Boulder, CO, USA, 1968.
6. Smith, R.V.; Randall, K.R.; Epp, R. *Critical Two-Phase Flow for Cryogenic Fluids*; NBS Technical Note 633; National Bureau of Standards: Washington, DC, USA, 1973.

7. Simoneau, R.J.; Hendricks, R.C. *Two-Phase Choked Flow of Cryogenic Fluids in Converging-Diverging Nozzles*; NASA Technical Paper 1484; Lewis Research Center: Cleveland, OH, USA, 1979.
8. Kieffer, S.W. Sound speed in liquid-gas mixtures: Water-air and water-steam. *J. Geophys. Res.* **1977**, *82*, 2895–2904. [[CrossRef](#)]
9. Henry, R.E.; Fauske, H.K. The two-phase critical flow of one-component mixtures in nozzles, orifices, and short tubes. *J. Heat Transf.* **1971**, *93*, 179–187.
10. Gopalakrishnan, S.; Schmidt, D.P. A computational study of flashing flow in fuel injector nozzles. *SAE Int. J. Engines* **2009**, *1*, 160–170. [[CrossRef](#)]
11. Battistoni, M.; Som, S.; Longman, D.E. Comparison of Mixture and Multifluid Models for In-Nozzle Cavitation Prediction. *J. Eng. Gas Turbines Power* **2014**, *136*, 061506. [[CrossRef](#)]
12. Lee, W.H. *A Pressure Iteration Scheme for Two-Phase Flow Modeling*; Technical Report LA-UR 79-975; Los Alamos Scientific Laboratory: Los Alamos, NM, USA, 1979.
13. Bilicki, Z.; Kestin, J. Physical aspects of the relaxation model in two-phase flow. *Proc. R. Soc. Lond. A* **1990**, *428*, 379–397.
14. Downar-Zapolski, P.; Bilicki, Z.; Bolle, L.; Franco, J. The non-equilibrium relaxation model for one-dimensional flashing liquid flow. *Int. J. Multiph. Flow* **1996**, *22*, 473–483.
15. Reocreux, M. Contribution a L'etude des Debits Critiques en Ecoulement Diphasique Eauvapeur. Ph.D. Thesis, Universit Scientifique et Medicale de Grenoble, La Tronche, France, 1974.
16. Banaszkievicz, M.; Kardas, D. Numerical calculations of the Moby Dick experiment by means of unsteady relaxation model. *J. Theor. Appl. Mech.* **1997**, *35*, 211–232.
17. Schmidt, D.P.; Gopalakrishnan, S.; Jasak, H. Multi-dimensional simulation of thermal non-equilibrium channel flow. *Int. J. Multiph. Flow* **2010**, *36*, 284–292. [[CrossRef](#)]
18. Travis, J.R.; Picconi Koch, D.; Breitung, W. A homogeneous non-equilibrium two-phase critical flow model. *Int. J. Hydrogen Energy* **2012**, *37*, 17373–17379. [[CrossRef](#)]
19. Venetsanos, A.G. Homogeneous non-equilibrium two-phase critical flow model. *Int. J. Hydrogen Energy* **2018**, *43*, 22715–22726. [[CrossRef](#)]
20. Wilhelmsen, O.; Aasen, A. Choked liquid flow in nozzles: Crossover from heterogeneous to homogeneous cavitation and insensitivity to depressurization rate. *Chem. Eng. Sci.* **2022**, *248*, 117176. [[CrossRef](#)]
21. Bellur, K.; Medici, E.F.; Hermanson, J.C.; Choi, C.K.; Allen, J.S. Modeling liquid-vapor phase change experiments: Cryogenic hydrogen and methane. *Colloids Surf. A Physicochem. Eng. Asp.* **2023**, *675*, 131932. [[CrossRef](#)]
22. Ferziger, J.H.; Peric, M. *Computational Methods for Fluid Dynamics*; Springer: Berlin, Germany, 1999.
23. Rodi, W. Experience with two-layer models combining the k- ϵ model with a one-equation model near the wall. In Proceedings of the 29th Aerospace Sciences Meeting, Reno, NV, USA, 7–10 January 1991.
24. Mulvany, N.; Tu, J.Y.; Chen, L.; Anderson, B. Assessment of two-equation modeling for high Reynolds number hydrofoil flows. *Int. J. Numer. Meth. Fluids* **2004**, *45*, 275–299. [[CrossRef](#)]
25. Hirt, C.W.; Nichols, B.D. Volume of fluid (VOF) methods for the dynamics of free boundaries. *J. Comput. Phys.* **1981**, *39*, 201–225. [[CrossRef](#)]
26. Wheeler, M.P.; Matveev, K.I.; Xing, T. Validation study of compact planing hulls at pre-planing speeds. In Proceedings of the 5th Joint US-European Fluids Engineering Summer Conference, Montreal, QC, Canada, 15–18 July 2018.
27. Matveev, K.I.; Wheeler, M.P.; Xing, T. Numerical simulation of air ventilation and its suppression on inclined surface-piercing hydrofoils. *Ocean Eng.* **2019**, *175*, 251–261.
28. STAR-CCM+ Manual. 2023. Available online: <https://mdx.plm.automation.siemens.com/star-ccm-plus> (accessed on 15 December 2023).
29. Bell, I.H.; Wronski, J.; Quoilin, S.; Lemort, V. Pure and pseudo-pure fluid thermophysical property evaluation and the open-source thermophysical property library CoolProp. *Ind. Eng. Chem. Res.* **2014**, *53*, 2498–2508. [[CrossRef](#)] [[PubMed](#)]
30. Leachman, J.W.; Jacobsen, R.T.; Penoncello, S.G.; Lemmon, E.W. Fundamental equations of state for parahydrogen, normal hydrogen, and orthohydrogen. *J. Phys. Chem. Ref. Data* **2009**, *38*, 721–748. [[CrossRef](#)]
31. Roache, P.J. *Verification and Validation in Computational Science and Engineering*; Hermosa Publishers: Albuquerque, NM, USA, 1998.

Disclaimer/Publisher's Note: The statements, opinions and data contained in all publications are solely those of the individual author(s) and contributor(s) and not of MDPI and/or the editor(s). MDPI and/or the editor(s) disclaim responsibility for any injury to people or property resulting from any ideas, methods, instructions or products referred to in the content.